Supporting Information

Catalyst discovery through megalibraries of nanomaterials

Edward J. Kluender,[1,2†] James L. Hedrick,[2,3†] Keith A. Brown,[2,4‡] Rahul Rao,[5,6] Brian Meckes,[2,4] Jingshan S. Du,[1,2] Liane M. Moreau, [1,2] Benji Maruyama[5], and Chad A. Mirkin[1-4*]

[†] These authors contributed equally.

*Corresponding author: Chad A. Mirkin, email address: chadnano@northwestern.edu

Characterization of spray profiles

The full width half max (FWHM) of radial spray distribution increased proportionally to the gun-sample separation distance in a manner such that the FWHM was 0.27 times the separation, which illustrates that this coating method could be readily adjusted to accommodate any array size (Fig. S1c). From this, adjustment of the gun distance and placement can be systematically done based on the array size (Fig. S1a).

Mechanism for ink drying

While spray-coating a uniform film on a flat surface is a well understood problem, forming a compositional gradient on a surface decorated with a periodic array of pyramidal tips could introduce problems stemming from inhomogeneous drying and diffusion of the constituent materials. Considering a small molecule with a diffusion constant D ~ 3.5×10^{-6} cm^2/s, one may estimate the time *t* over which molecules will diffuse a distance *x* using a diffusion equation $t = x^2/2D$ (1). In particular, for a 1.5 cm wide pen array with a pen-to-pen pitch of 120 μm, the molecule will diffuse between pens in ~20 s and across the whole array in ~400 days, suggesting an extremely long window over which drying can occur and still maintain the compositional gradient. Importantly, we hypothesize that allowing for enough time for diffusion to occur around a specific pen may be very important as it could allow for localized diffusive mixing of the multicomponent ink sprayed near a given pen (Fig. S2) (2,3).

Composition determination via X-Ray Fluorescence

Qualitatively, it is observable (Fig. S6) that going from the Au-rich (right) to Pd-rich (left) side of the substrate, the Au Lβ fluorescence intensity decreases while the Pd Kα fluorescence intensity increases as would be expected (Fig. S7). Quantitative analysis of the Au and Pd relative atomic percentages were conducted using corrected areas under the Pd Kα (21177 eV) and Au Lβ (11443 eV) fluorescence lines, with peak areas fit to a Gaussian distribution after background subtraction using Origin 8.6 graphing software. Intensity values were corrected for dead-time, incident beam intensity, elemental cross-sections (4), detector efficiency, and attenuation due to species present between the sample and detector at the relative fluorescence line energies.

www.pnas.org/cgi/doi/10.1073/pnas.1815358115

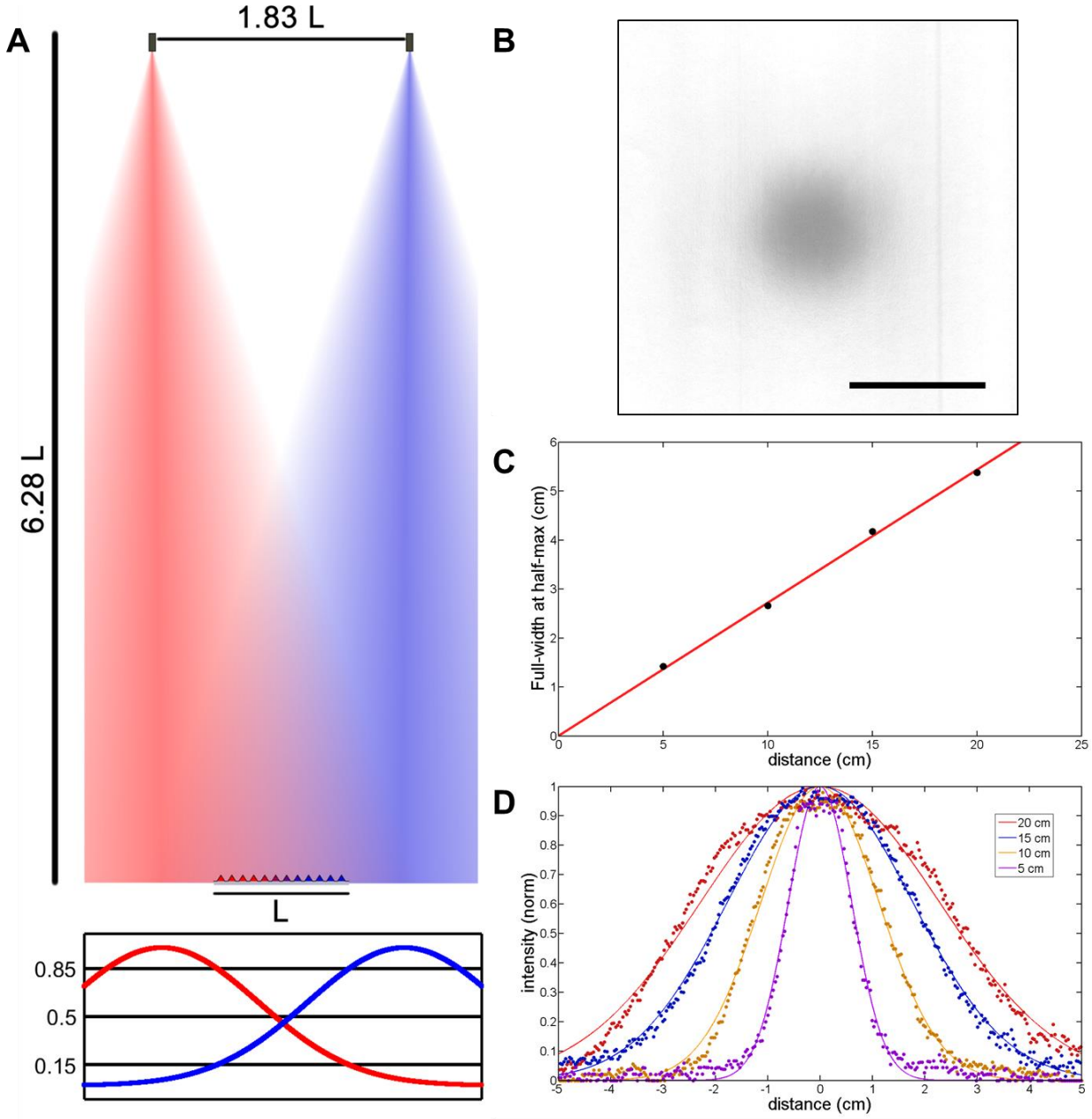

Fig. S1: Scalability of spray-coating with different arrays. (A) Diagram of how to position spray guns to PPL array based on size, (B) scanned spray used to quantify intensity, scale bar 5 cm (C) linear full width half max slope showing a linear scaling trend for PPL arrays, (D) equation fitting of spray intensity data at different distances.

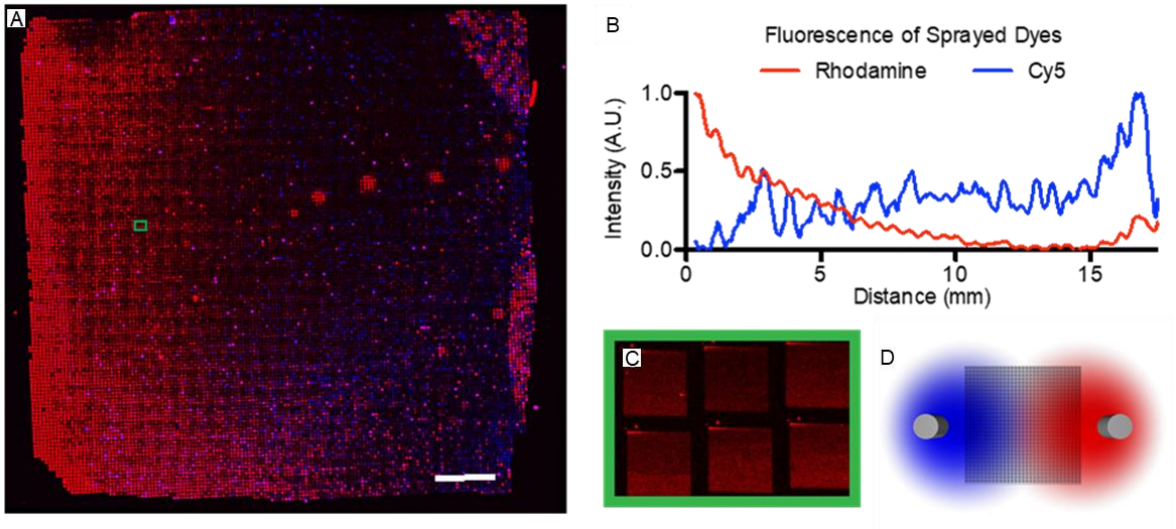

Fig. S2: Large scale gradients of patterned nanomaterials. (A) Stitched confocal fluorescence image of a compositional gradient of two different fluorophores in patterned polymeric domes, scale bar is 2 mm, and (B) fluorescence intensity across of each region. (C) A magnified fluorescence image showing a single tile from (A), illustrating the dot arrays pattern, as well as the resolution of (A). (D) Schematic of the airbrush position during spraying.

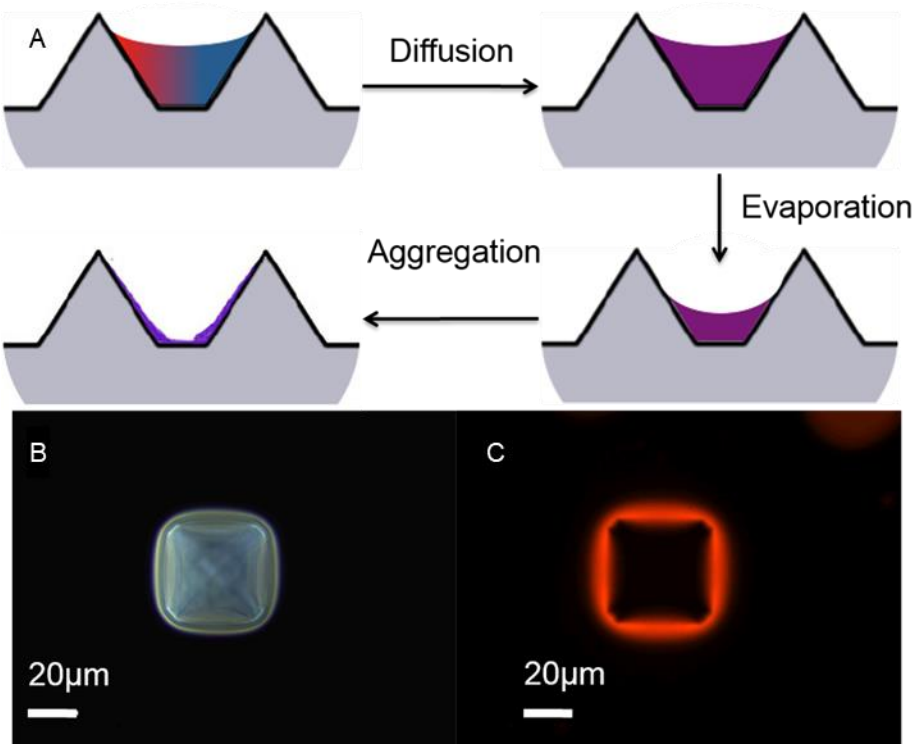

Fig. S3: Evaporative self-assembly of diffused ink around pyramidal pens. (A) Proposed mechanism of ink evaporation following spray coating in which evaporation and diffusion leads to homogenous mixing of the inks and preferential deposition of the ink on the pens. Optical image of a single pen under (B) dark field and (C) fluorescence showing preferential inking at the base of the pen.

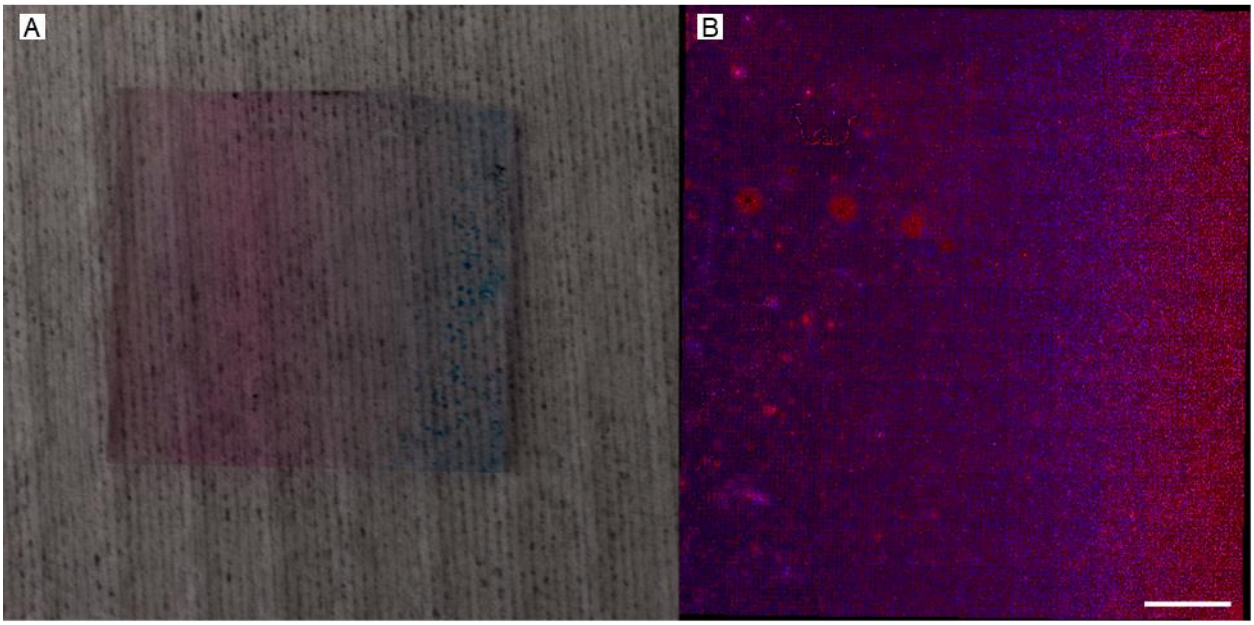

Fig. S4: PPL array spray-coated with a composition gradient. (A) Photograph and (B) confocal micrograph of the composition gradient spray coated onto the PPL array.

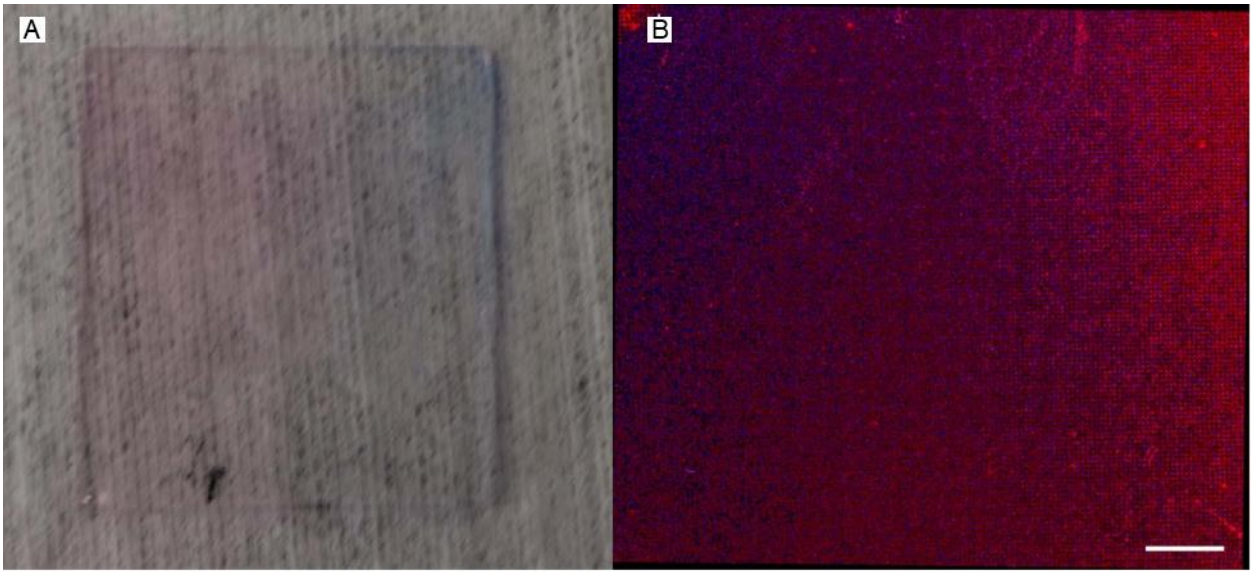

Fig. S5: PPL array spray-coated with both a size and composition gradient. (A) Photograph and (B) confocal micrograph of the composition and volume gradient spray coated onto the PPL array, which results in a composition and size gradients when patterned.

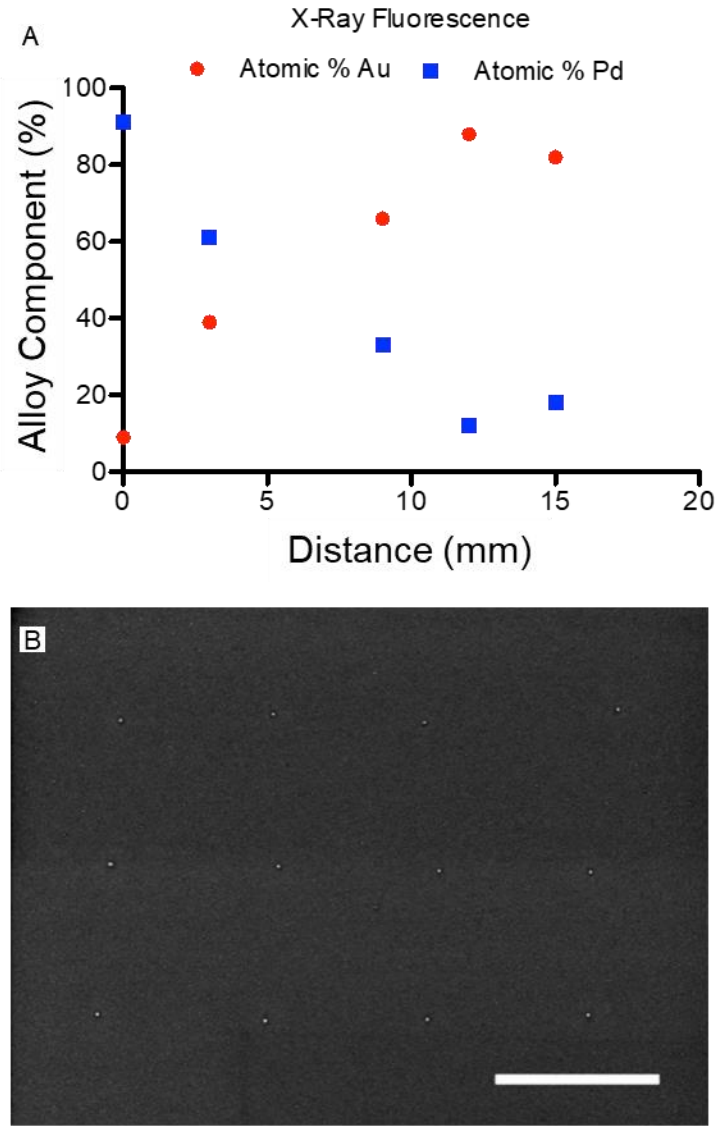

Fig. S6: 14 million bimetallic nanoparticles synthesized in parallel with a compositional gradient. (A) X-ray fluorescence profile of Au-Pd alloy composition of SPBCL patterned array taken with a 3 mm slit, note that the last point is at the edge of the array. (B) SEM of SPBCL Au-Pd nanoparticles. Scale bar is 2 µm.

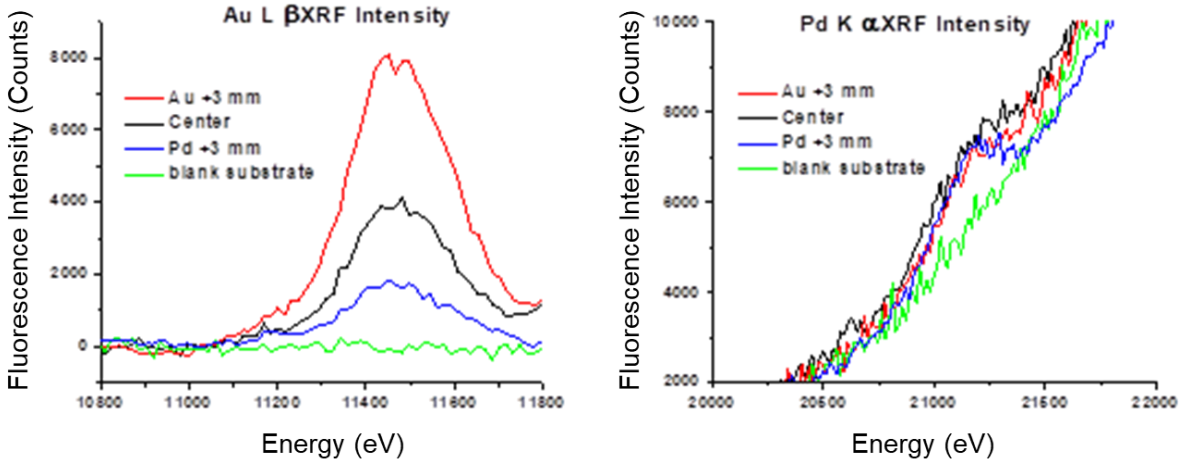

Fig. S7: Au Lβ and Pd Kα Fluorescence Intensities. The Au Lβ fluorescence line intensity (left) increases towards the Au-rich side of the sample and decreases towards the Pd-rich side. No signal is observed for the case of a blank substrate (green). The Pd Kα fluorescence line intensity (right) decreases towards the Au-rich side of the sample and increases to a well-defined peak (blue) towards the Pd-rich side of the spectrum. +3 Au refers to a 3 mm offset from the sample center towards the Au-rich (right) side, and +3 Pd refers to a 3 mm offset from the sample center towards the Pd-rich (left) side.

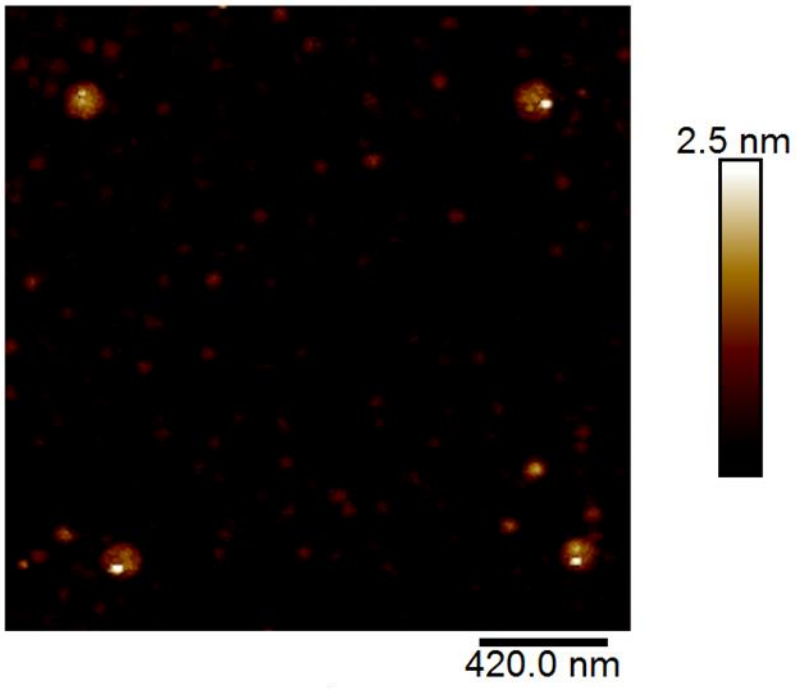

Fig. S8. AFM of AuCu particles in catalytically active size regime prior to calcination. AFM of AuCu particles on top of ARES micropillar with heights of ~2.5 nm. This AFM was performed prior to calcination with residual carbon from the patterned polymer nanoreactor still present surrounding each nanoparticle.

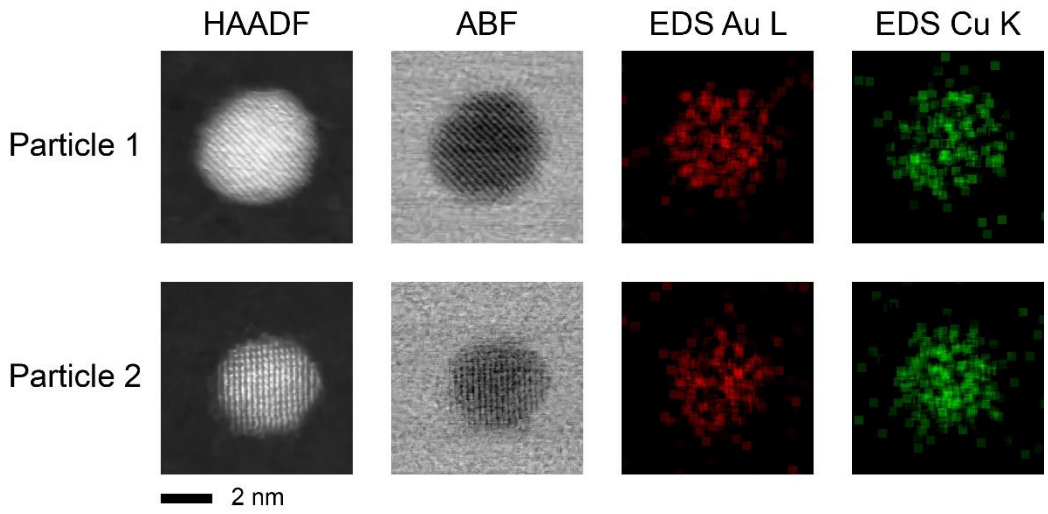

Fig. S9: Scanning transmission electron microscopy of Au-Cu alloy nanoparticles in catalytically active size regime. The particles were synthesized on an electron-transparent silicon nitride thin film but have similar sizes as the ones on ARES micropillars and show a homogenous alloy structure. From left to right: high-angle annular dark field (HAADF) images, annular bright field (ABF) images, energy-dispersive X-ray spectroscopy (EDS) elemental mapping results for Au L and Cu K lines. All images share the same scale bar of 2 nm. HAADF and ADF images were denoised using the block-matching and 3D filtering (BM3D) method (5).

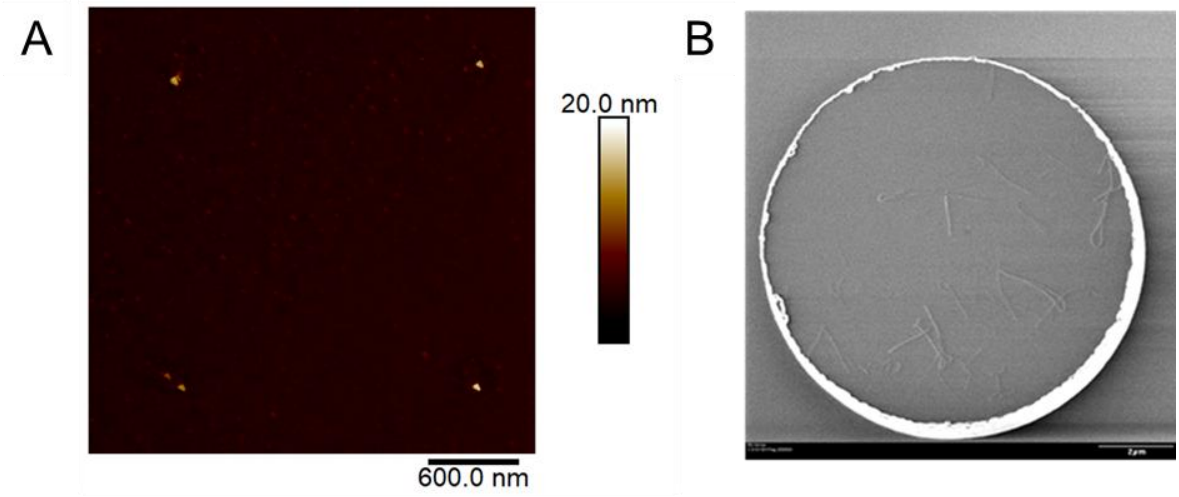

Fig. S10: Multiwalled CNTs grown from large particles. (A) AFM of patterned Au nanoparticles post-heat treatment and calcination. Particles are ~10 nm tall. (B) SEM of CNTs grown in ARES showing large diameter tubes. Additionally, *ex situ* Raman spectra were collected and no RBMs were observed indicating the presence of MWNTs.

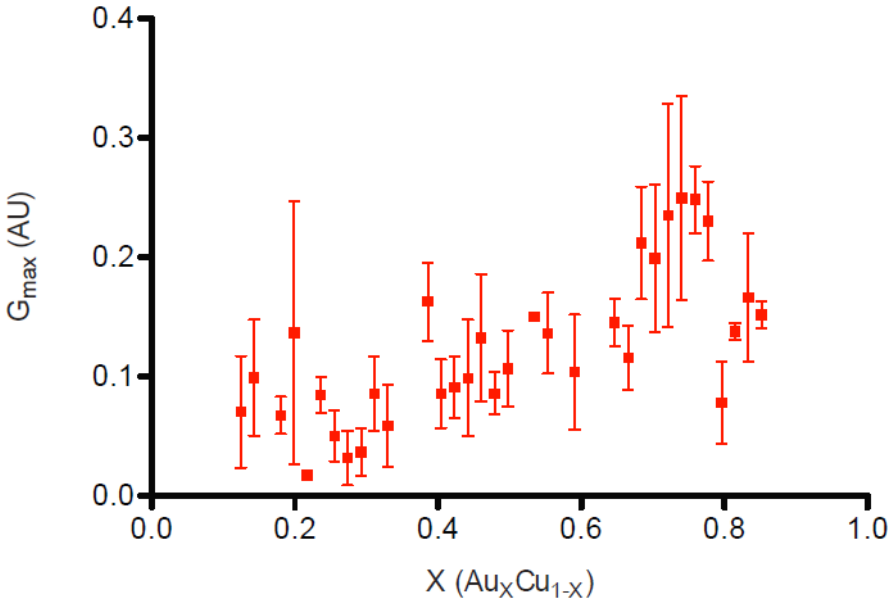

Fig. S11: Compositional breakdown of growths performed at 800-900 ºC. Integrated intensity of the SWNT Raman G-band as a function of catalyst composition. The data is normalized to the same scale as Fig. 4. Growths produced fewer SWNTs at all compositions, but still exhibited increased growth at x= ~0.75.

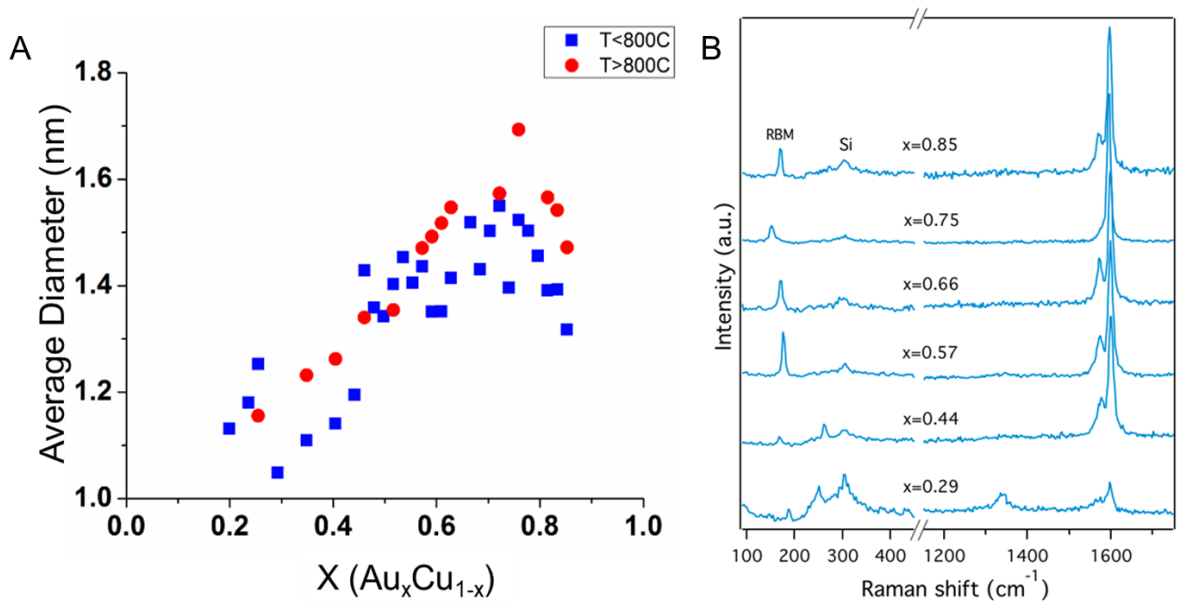

Fig. S12: Average SWNT diameter as a function of Au content. RBMs were collected across the compositional array. The diameter of a SWNT is inversely proportional to the RBM (d=248/RBM). It has been shown previously that average particle size increases with Au content owing to the larger lattice constant of Au compared to Cu (6). In this study, we kept the molar metal loading constant across our gradient, yet we observed that the average SWNT diameter increases with Au content (A), which may be attributed to an increase in lattice constant. (B) Representative Raman spectra, with RBM region included, across the composition range exhibiting frequency shifts in RBM peaks that coincide with an increase in diameter as a function of Au content.

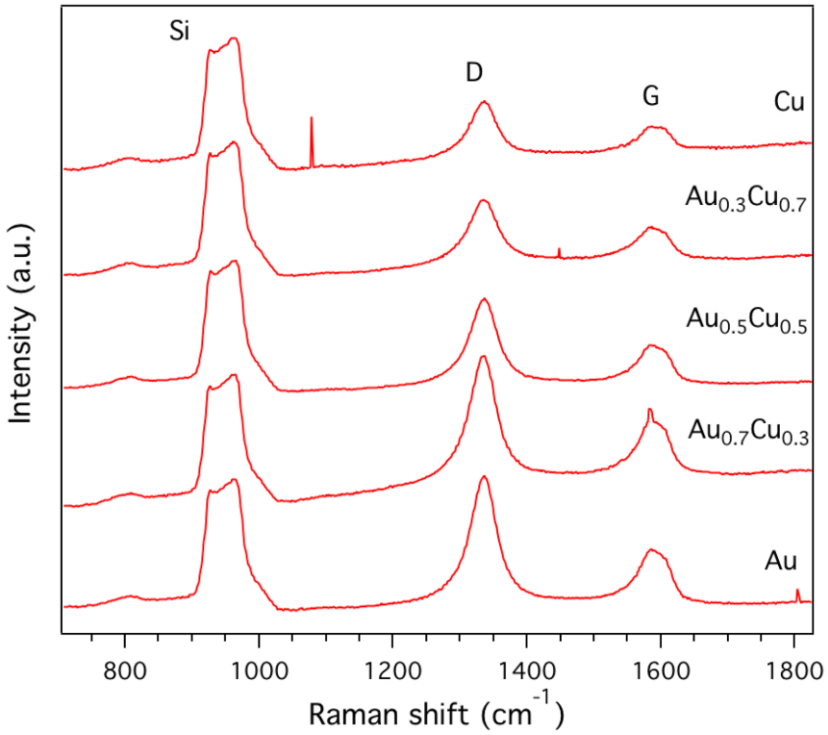

Fig. S13: Raman spectra of SWNTs grown from dip coated catalyst. Raman spectra exhibit similar trends to those seen in SPBCL ARES spectra, with an increased catalytic activity at ~Au_3Cu.

References Cited in SI

1. Shimizu T, Kenndler E (1999) Capillary electrophoresis of small solutes in linear polymer solutions: Relation between ionic mobility, diffusion coefficient and viscosity. *Electrophoresis* 20:3364–3372. Q:22
2. Su G, Guo Q, Palmer RE (2003) Colloidal lines and strings. *Langmuir* 19:9669–9671.
3. Bowden N, Brittain S, Evans AG, Hutchinson JW, Whitesides GM (1998) Spontaneous formation of ordered structures in thin films of metals supported on an elastomeric polymer. *Nature* 393:146–149.
4. Puri S, et al. (1995) K and L shell X-ray fluorescence cross sections. *At Data Nucl Data Tables* 61:289–311.
5. Dabov K, Foi A, Katkovnik V, & Egiazarian K (2008) Image restoration by sparse 3D transform-domain collaborative filtering. *Proc. SPIE* 6812:681207.
6. Motl NE, Ewusi-Annan E, Sines IT, Jensen L, Schaak RE (2010) Au−Cu alloy nanoparticles with tunable compositions and plasmonic properties: Experimental determination of composition and correlation with theory. *J Phys Chem C* 114: 19263–19269.